Rocky Worlds DDT: JWST Data Analysis Report for GJ 3929 b

Douglas Long, Ian Wong, and Taylor J. Bell
JWST Data Analysis Team
March 17, 2026

1 Observation Overview

Under the RWDDT program, JWST-DDT-9235 Observation 3 obtained time-series imaging of the third eclipse of GJ 3929 b using MIRI/F1500W with the SUB128 subarray, covering 6.17 hours, with the goal of measuring the secondary eclipse of the planet. No attempt is made here to incorporate data from the previous 2 observations to improve measurement of the eclipse depth or timing. High Level Science Products (HLSPs) from this observation are hosted on MAST and include both intermediate and final results to help drive research-community engagement.

We measured both the centroid position and width of the target's point-spread function (PSF) during each integration. The telescope pointing remained quite stable along the x and y axes throughout the observation, but the width of the PSF along both axes increased smoothly during the first $\sim$1 hour of the observation before settling to a stable value (see Figure 1). A decrease in the raw flux is seen during the first $\sim$1 hour as well.

2 Data Reduction

This report presents results from two independent reductions and analyses performed by Analyst A (Long) and Analyst B (Wong). Both analyses used the standard JWST pipeline (`jwst` v1.20.2 with CRDS context `jwst_1464.pmap`) for detector-level calibrations. Stage 1 processing included running the following steps: `emicorr`, `saturation`, `firstframe`, `lastframe`, `reset`, `linearity`, `rscd`, `dark_current`, and `jump` (with the threshold increased from 4.0 to 8.0). In Stage 2 we ran the `flat_field` step, but we disabled the `photom` step as flux-calibrated data are not desired for time-series analyses.

Photometric extraction and light curve fitting were completed using Stages 3–5 of the `Eureka!` Python package (v1.4.dev106+g3a6724481). Analyst A chose to work with a cut-out portion of the subarray that excluded rows and columns along the edges where most pixel values were marked as `NaN`. A time series was constructed for each pixel, and 5σ outliers (along with all `NaN` values) were replaced using bilinear interpolation over the nearest neighbors. Next, a center-of-mass centroid was calculated for each integration using the 'mgmc' method within `Eureka!`'s Stage 3. The position and width of the target's PSF along the x and y axes were measured in each integration using a 2D Gaussian fit (see Figure 1).

Photometric light curves were extracted in Stage 3 of `Eureka!` using the `photutils` package with circular apertures and 'exact' edges, where pixels are weighted by the fraction of their area lying within the specified aperture. A range of aperture and background

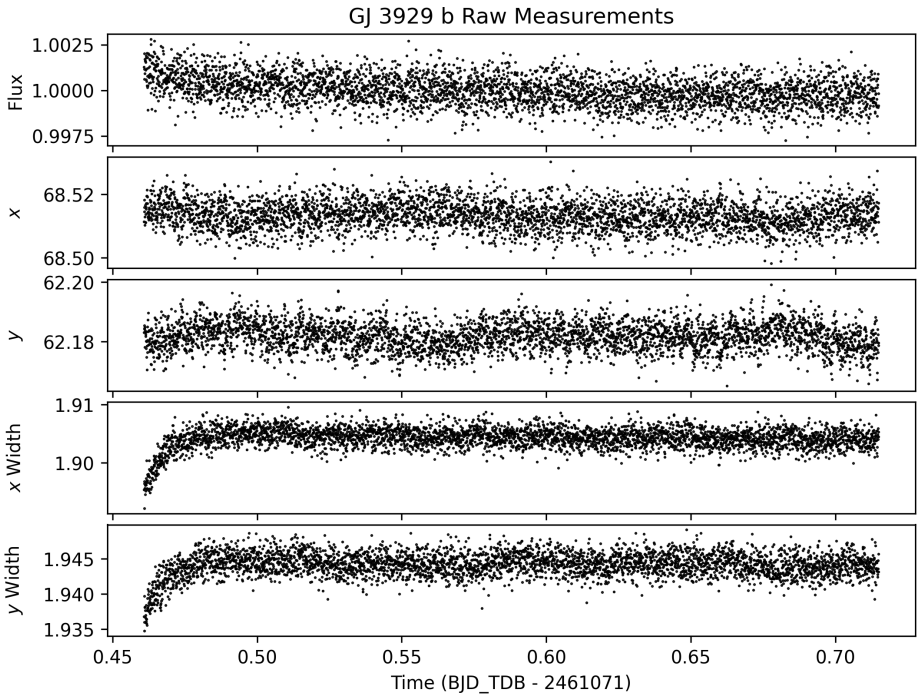

Figure 1: Stability of flux, centroid, and PSF. Time series of changes in the normalized raw flux, centroid position (x, y), and PSF width (computed as a Gaussian standard deviation along the x and y axes), illustrating initial settling behavior and overall pointing stability.

annulus radii were considered. Aperture radii ranged from 4–11 pixels, in 1-pixel steps. The inner radius of the background annulus varied from 14 to 26 pixels in 4-pixel steps, while the annulus width ranged from 10 to 30 pixels in 10-pixel steps. Photometric light curves were generated for each source aperture + background annulus pair. Both analysts chose to reject any integrations lying 3.5σ away from the rolling median using a boxcar filter with a width of 20 integrations.

3 Light Curve Fitting

The most obvious feature in all of the extracted light curves is the large ramp during the first $\sim$1 hour of the observation. The two analysts chose to deal with this in slightly different ways. Analyst A trimmed off only the first 50 integrations, then used an exponential function in their light curve fit. Analyst B took advantage of the long baseline before the predicted eclipse ingress time and trimmed the first 800 integrations.

Initial fits were done using the PSF centroid positions (x, y) and widths (sx, sy) as lienar detrending vectors. We found that the Bayes factor strongly favored removing x and y from our fits. The final fit results only used the PSF widths as detrending vectors. There is also an overall monotonic decrease in flux across the entire observation that was fitted with a linear trend in time.

Often, modeling systematic noise using detrending vectors and simple temporal trends is not enough to remove time-dependent 'red' noise from the light curve. To test this, the

light curves were fit both with and without the inclusion of a `celerite2` Gaussian Process (GP) with a Matérn-3/2 kernel as a function of time to model low-level red noise. Both analysts found no evidence for significant red noise in the residuals from the best-fit models without GP, and therefore the GP was not included for deriving the final results presented in this report.

Fits made using a wide Gaussian prior on the eclipse time ($\sigma_t = 0.1$ d) yielded a bimodal distribution in eclipse depth vs. eclipse time, with one cluster in eclipse time centered near the predicted circular orbit eclipse time and the other that was situated after the end of the time series. For cases in which the best-fit eclipse time occurred after the end of the time series, the eclipse depth was also consistently negative; it seemed to us that the sampler was trying to fit the egress of the 'positive' eclipse signal with an ingress for a 'negative' eclipse signal. As a result, Analyst B also tried a 'medium'-width prior of ($\sigma_t = 0.025$ d) which greatly reduced the number of 'negative' eclipse results. A narrow prior ($\sigma_t = 0.0015$ d) assuming a circular orbit was also tested. Analyst A selected the narrow prior for their fiducial analysis, while Analyst B utilized the medium-width prior.

All priors for the astrophysical and systematic models for our fiducial fits are summarized in Table 1. Our model can be summarized as:

$$\mathrm{Model}(t) = E(t) * S(t),$$

where $E(t)$ is the batman eclipse model, and $S(t)$ is the composite systematic noise model, defined as

$$S(t) = P(t)R(t)SY\Big(sy(t)\Big)SX\Big(sx(t)\Big), \tag{1}$$

where

$$P(t) = c_0 + c_1(t - \bar{t})$$

is a linear trend in time where $\bar{t}$ is the mean time, and

$$R(t) = 1 + r_0 \exp\Big(-r_1(t - t_{\mathrm{start}})\Big)$$

is an exponential ramp, with t_{start} defined as the time of the first integration. Analyst B did not include an exponential ramp in their fits, i.e., $r_0 = 0 => R(t) = 1$.

SX and SY are linear decorrelation functions defined similarly to each other as

$$SX\Big(sx(t)\Big) = 1 + c_{sx}\Big(sx(t) - \overline{sx}\Big)$$
$$SY\Big(sy(t)\Big) = 1 + c_{sy}\Big(sy(t) - \overline{sy}\Big)$$

where ($sx(t)$, $sy(t)$) are the PSF width along the x and y axes as a function of time, and ($\overline{sx}$, $\overline{sy}$) are the corresponding mean values across the time series. Lastly, we also included a white noise scaling factor, `scatter_mult`, as a multiplier to the photometric uncertainties estimated during the Stage 3 reduction.

Table 1: The astrophysical and systematic model priors for the fits assuming a circular orbit. Fixed astrophysical parameters are shown without uncertainties and provided by the juliet$_{circ}$ fit from the CIT's orbit fitting efforts during observational scheduling.

Parameter	Prior
P	2.6162644 days
$t_{\rm sec}$	$\mathcal{N}(2460765.0434, 0.0015 \text{ OR } 0.025)$ BJD$_{\rm TDB}$
b	0.20
a/R_*	17.26
e	0
R_*[†]	0.315
$R_{\rm p}/R_*$	0.03045
$F_{\rm p}/F_*$	$\mathcal{N}(100, 300)$ ppm
c_0	$\mathcal{N}(0.999, 0.01)$
c_1	$\mathcal{N}(0.0, 0.1)$
r_0[‡]	$\mathcal{N}(0.0, 0.1)$
r_1[‡]	$\mathcal{U}(3, 300)$
c_{sx}	$\mathcal{N}(0.0, 0.5)$
c_{sy}	$\mathcal{N}(0.0, 0.5)$
scatter_mult	$\mathcal{U}(0.8, 10)$

[†]The stellar radius is used to account for the difference in light travel time throughout the planet's orbit.
[‡]Only Analyst A chose to use the exponential ramp model, with Analyst B effectively having fixed r_0 to 0.

3.1 Results & Discussion

Each of the two analysts chose their own criteria to determine their final preferred reduction and light curve fit. These are shown in Table 2. Analyst A selected the aperture radius that had the lowest photometric noise, i.e., lowest scatter in the residuals from the Stage 5 light-curve fit. The same considerations were taken to select the background annulus radius and width. This result was cross-checked by examining the fitted eclipse depth uncertainties as function of radii. Analyst B found that aperture radii of 4–6 pixels yielded a larger variance in eclipse depth uncertainties than those with radii of 7 pixels or larger. After discarding the smaller apertures, they selected the aperture and background annulus combination that yielded the smallest eclipse depth uncertainty. Despite these different approaches, the measured eclipse depths from the two analyses agree at better than 1σ. The mid-eclipse time obtained by Analyst B, which was estimated using the medium-width eclipse time prior, is within 2σ of the value measured by Analyst A assuming a nearly circular orbit. Notably, the mid-eclipse time measurement from Analyst B is not prior-dominated, indicating that the MIRI light curve is providing some constraint on the eclipse timing. Neither analysis found any significant amount of residual red noise, and both are broadly consistent with the maximum expected eclipse depth of $\sim$134 ppm, which assumes zero albedo and no atmospheric recirculation. The standard deviation of the light-curve residuals for both analyses is $\sim$745 ppm.

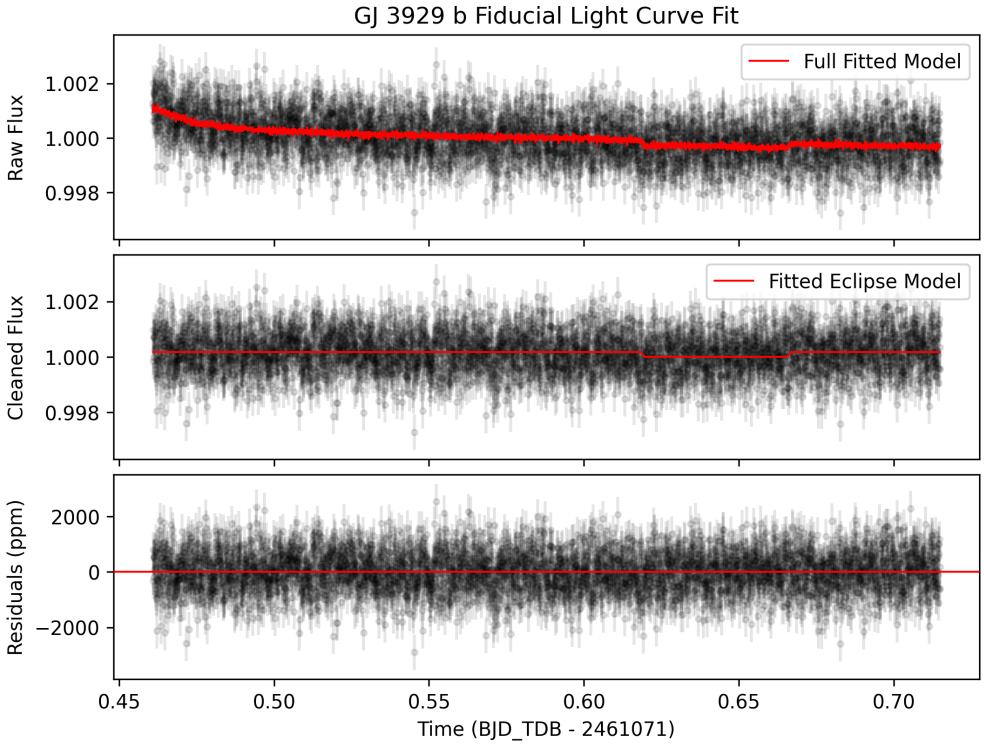

Figure 2: Fiducial light curve fit. *Top:* the raw, normalized flux measurements in black with the best-fit combined systematics and eclipse model overplotted in red. The first 50 integrations were excluded from the fitting analysis. *Middle:* the systematics-divided flux measurements are shown in black, with the fitted eclipse model shown in red. *Bottom:* the corresponding residuals.

4 Calibrated Stellar Flux Measurement

Following the methodology of Gordon et al. (2025), we measured absolutely-calibrated stellar photometry using `calints` FITS files with a 5.69 px aperture and an 8.63–11.45 px background annulus, applying an aperture correction of 1.497. Adding in quadrature the observational scatter with the $\sigma(\mathrm{CF}) = 0.48\%$ and $\sigma(\mathrm{repeat}) = 0.45\%$ terms from Gordon et al. (2025), we obtained a calibrated stellar flux of 18.86 ± 0.12 mJy.

The calibrated stellar flux for this observation is ∼10% higher than that measured for Observations 1 and 2. This is due to an overly aggressive bad pixel mask supplied in CRDS context `jwst_1364.pmap` that was used by the analysts of Observations 1–2;

Table 2: Fiducial eclipse fit results for GJ 3929 b.

	Eclipse Depth [ppm]	t_{sec} [$\mathrm{BJD_{TDB}}$]	Residual Std. Dev. [ppm]
Analyst A†	174^{+34}_{-40}	$2460765.0397^{+0.0011}_{-0.0013}$	742 ± 8
Analyst B	186^{+33}_{-34}	$2460765.0371^{+0.0009}_{-0.0020}$	749 ± 9

†Our fiducial analysis, whose final and intermediate data products are hosted on MAST as an HLSP.

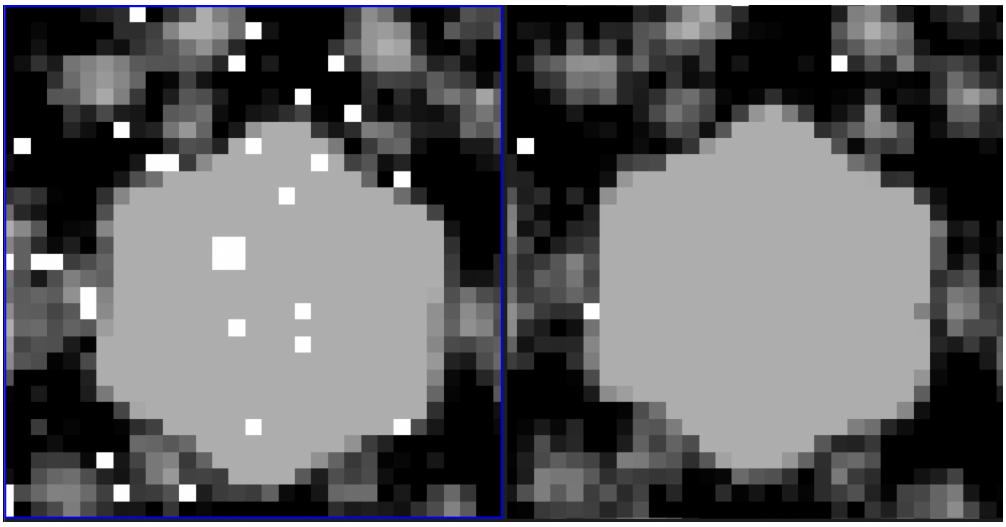

Figure 3: Effects of different bad pixel masks *Left:* Observation 2, which used CRDS `jwst_1364.pmap`, had a number of flagged pixels on the PSF, including the 4 adjacent to one another in the upper left center. *Right:* Observation 3 (this work) uses CRDS `jwst_1464.pmap` which has no clumps of bad pixels on the target PSF.

specifically, multiple pixels within or near the central core of the PSF of stars placed on the nominal pointing position of the SUB128 subarray were set to DO_NOT_USE. The bilinear interpolation over those flagged pixels was likely especially poor due to the presence of a 2×2 block of bad pixels within the source aperture, yielding a lower measurement of the total flux (see Figure 3). Updated versions of the HLSPs for Observations 1–2 will be posted, using the newer `jwst_1464.pmap`, which should improve the absolutely-calibrated stellar photometry.

5 Discussion and Outlook

This report provides a **snapshot** of GJ 3929 b from a single observation. The relatively low uncertainties on a potential eclipse are tantalizing, but the inclusion of additional eclipses is needed to more accurately constrain the eclipse depth and timing. This observation tentatively favors a nearly circular orbit but cannot rule out a larger eccentricity. For community analysts, the reduction/fitting configurations and noise benchmarks presented here offer a practical starting point; for modelers, the preliminary depths/timings and robust stellar flux measurements enable early exploration of different atmospheric and/or surface scenarios.